An interface interaction method for compressible multifluids

Xiang Yu Hu and Boo Cheong Khoo

Singapore-MIT Alliance, National University of Singapore, 4 Engineering Drive 3, 117576, Singapore

Abstract

In the development of numerical schemes for compressible multifluids, the treatment of the interface is very important. In this paper, we proposed a numerical method based on interface interactions where the interface conditions are determined by the real interface interactions and the ghost cell states by hypothetical "ghost" interactions. We construct the algorithm based on the ghost fluid method (GFM) (Fedkiw et al, 1999b). A level set function is used to track the interface with further modification to the re-initialization procedure to achieve higher accuracy. Extensive tests in 1D are carried out and with the 2D examples suggest that the present scheme possesses greater robustness than the original GFM while still keeping to its simplicity.

1 Introduction

Various numerical methods have been developed to simulate and study the dynamics of compressible multifluids in a wide range of high speed flow phenomena, such as the dynamics and the stability of shock interface interaction, supersonic mixing processes, high speed bubbly flows, underwater explosion and many others. Invariably, a relative dominant difficulty for these numerical computations is the treatment of material interfaces. For Eulerian schemes, in general, there are two main approaches: one is the rather complicated front tracking method in which the interface is tracked as an internal moving boundary and a non-smeared interface can be materialized; the other is the relatively simple front capturing method in which the interface is defined as a steep gradient and hence the latter is allowed to be smeared over a narrow band. Good summaries on multifluids interface treatment may be found in Abgrall and Karni (2001) and Glimm et al(1999).

To obtain a non-smeared interface and avoid the complexity of front tracking,

the employment of level set function enables a combination of the above two methods (Osher and Sethain, 1988), in which the interface is treated as inner boundaries and the front movement is captured by a level set function. In the original work by Mulder et al (1992), the interface is still allowed to be smeared to a certain thickness artificially. In Davis (1992), Cocchi and Saurel (1997) and Liu et al (2001a, 2001b), smearing at the interface is avoided by solving the Riemann problem to correct for the numerical flux near the interface. However, as noted by Fedkiw et al (1999b), these schemes can be and is usually fairly intricate and can perhaps only be extended to multidimension with dimensional splitting in time.

The ghost fluid method (GFM) (Fedkiw et al, 1999b), on the other hand, presents a fairly simple way to implement in multidimension and with multilevel time integrals. The GFM, however, faces some difficulties when there are large differences of states or material properties at the interface. In these said cases, the thermodynamically similarity of the "ghost fluid" cells can not be assured and the method may suffer from large error or serious oscillations near the interface (Liu et al, 2002). Abgrall and Karni (2001) proposed another similar but simpler single fluid method (SFM). However, the SFM may not be suitable when there is density limitation in the equation of states like Tait's equation for the water medium. As will be shown in this paper, SFM encounters essentially the same difficulties as the GFM. Fedkiw (2002) presented a modified GFM for the air-water interaction which eliminates the oscillations at the air-water interface. However, this modified GFM seems to be air-water interaction specific such that there is a very large sound impedance change across the interface. Recently, Liu et al (2002) proposed a method which requires solving the full Riemann problems near the interface. In order to avoid serious oscillations, the proposed interface states for the associated Riemann problems have to be applied to locations having some distance from the interface. Therefore, this method may give rise to difficulties in maintaining accuracy at the interface and is also relatively much less straightforward in its implementation and extension to multidimension problems with complex interfaces.

The motivation of this paper is to overcome the difficulties faced by the original GFM or even the modified GFM when large differences of states and material properties occur at the interface via construct a *new* GFM based on the interface interaction. All the while, it is imperative that the method still keeps to the simplicity of the original GFM. Based on the present method, we also propose an improved treatment of the re-initialization step in the level set function calculation for general interface so as to increase the accuracy of the interface location update.

2   Preliminaries

2.1   Euler equations

Assuming the fluid is inviscid and compressible, the flow can be described by Euler equations in two dimensions

$$
\begin{pmatrix} \rho \\ \rho u \\ \rho v \\ E \end{pmatrix}_t + \begin{pmatrix} \rho u \\ \rho u^2 + p \\ \rho uv \\ (E+p)u \end{pmatrix}_x + \begin{pmatrix} \rho v \\ \rho uv \\ \rho v^2 + p \\ (E+p)v \end{pmatrix}_y = 0, \tag{1}
$$

This set of equations describes the conservation of density ρ, momentum $\rho \mathbf{v} \equiv (\rho u, \rho v)$ and total energy density $E = \rho e + \frac{1}{2}\rho u^2$, where e is the internal energy per unit mass. The one-dimensional Euler equations are obtained by setting $v = 0$.

To close this set of equations, the equation of states (EOS) must be defined to give the relation between pressure, density and internal energy. There are several forms of EOS for different materials, but all can be written generally as $p = p(\rho, e)$. If the entropy is kept constant, an isentropic EOS results and can be written as $p = p(\rho, s_0)$. Here, the pressure is determined by density directly.

2.2   Level set equation

Consider a moving interface $\Gamma(t)$ separating the domain $\Omega(t)$. We associate $\Omega(t)$ with a signed distance function $\phi(x, y, t)$, that is $\nabla|\phi| = 1$, called the level set function (Osher and Sethain, 1988). Knowing ϕ we may locate the interface by finding the zero level set of ϕ. That is $\Gamma(t) = \{x, y : \phi(x, y, t) = 0\}$. So the movement of the interface is equivalent to the updating of ϕ. We can use the level set equation

$$
\phi_t + u\phi_x + v\phi_y = 0 \tag{2}
$$

to update all the level sets, where u and v are the velocity components for the level sets in x and y directions.

For compressible multi-material flows, the interface velocity is usually not known, hence the movement of the zero level set at interface is approximated

by updating level sets on the nearest grid points. As the speed near the interface may change very rapidly or become a discontinuity as the interface moves, the solution of Eq. 2 often becomes very flat and/or steep at the interface. Therefore, ϕ needs to be re-initialized to be kept as the signed distance. The re-initialization equation can be written as

$$\phi_\tau + sgn(\phi)\left(|\nabla\phi| - 1\right) = 0, \tag{3}$$

where $sgn(\phi)$ is a sign function and is usually approximated by a smooth function (Peng et al, 1999). For a given ϕ, this equation can be solved to steady state. As re-initialization is needed for the whole domain, the fast marching method (Sethain, 1999) can also be used to increase efficiency, in which case the eikonal equation $|\nabla\phi| = 1$ is solved directly. For the flows with strong shock waves, ϕ may need to be re-initialized at every time step. However, re-initialization at every time step can lead to the movement of the zero level set and must be performed extremely carefully; otherwise serious difficulties will result, such as large mass loss.

In the computation of compressible multifluids, smooth or constant extension of a quantity q is sometimes needed. For example, in the GFM, flow variables are needed to be extended into the ghost cells. We use the extending equation

$$q_\tau \pm \mathbf{N} \cdot \nabla q = 0 \tag{4}$$

to extend quantities to their neighborhood. Here $\pm\mathbf{N}$ is the positive and negative normal direction of the level set and used to decide the extending direction (Peng et al, 1999). $+\mathbf{N}$ is used to extend quantities from regions $\phi < 0$ to regions $\phi > 0$, while $-\mathbf{N}$ is used to extend quantities from regions $\phi > 0$ to regions $\phi < 0$. Again, for a given q, the extending equation can be solved to steady solution.

2.3   *Ghost cells*

As the interface serves to separate two distinct media, the two associated flow fields are to be solved separately. In a finite difference implementation, special care is needed when the grid points of the difference stencil is cut by the interface. As such, the states on the other side of the interface can not be used directly which can and usually leads to serious oscillations. These "missing" points can be filled by the so called ghost cells (collocated with the real cells but separated by the interface). Therefore, both the two fluids have their own real cells and ghost cells. The presence of ghost cells allows the two fluids to be calculated separately as a single fluid and makes the interface "invisible" during the computation.

The ghost cell can be considered to be first introduced to the front tracking method by Glimm et al (1981), in which the states of the ghost cells are extrapolated from nearby point from the same side. For the GFM based on level set tracking (Fedkiw et al, 1999b), a narrow band of ghost cells is defined in the vicinity of the interface. At the ghost cells, the ghost fluid is defined with the same pressure and normal velocity of the real fluid and the ghost cell density is obtained from isobaric fixing technique. For the SFM, the ghost cells are defined by directly copying the pressure, normal velocity and density from the real cells. In the modified GFM (Fedkiw 2002) for the air-water interaction, the normal interface velocity is obtained from the water side and the pressure at the interface is obtained from the air side.

3   The interface interaction method

In our method, the ghost cell states are defined according to the interface interactions. We firstly determine the interface condition. That is, the interface velocity, pressure and densities are obtained by solving the real interface interaction of the two fluids. Then two hypothetic interactions called *ghost interactions* are defined between each ghost fluid to its corresponding real fluid. In each ghost interaction, the real fluid reaches the same interface condition as that of the real interaction. As higher order extrapolation may be used to calculate more accurate states near the interface, the interface condition can also be obtained with higher order accuracy by involving more nodes. Hence, the ghost cell states are also correspondingly evaluated. Therefore, the present method can lead or be extended to a possible higher order for multifluids problems. However, for simplicity, the discussion in this paper is based on the first order extrapolation only.

Usually, there are many ways, based on different assumptions, to solve the interface interaction, such as the exact Riemann solver and approximate Riemann solver. In this paper, both the real and ghost interactions at the interface are solved by the method of characteristics (Rudinger, 1969). For this method, we propose two assumptions: *a*) the interactions take place on the two fluid nodes nearest to the interface, *b*)the interactions are isentropic processes in which there is no entropy change for the two respective fluids or any entropy exchange between them throughout the interaction. The first assumption is to ensure that the interaction process is totally controlled by the two fluid states nearest the interface and any other flux into the interaction region is neglected. For the second assumption, no heat transfer and mass diffusion is allowed.

3.1 Interface condition

Assume that the adjacent grid cells have two different fluids and their states are $W_j = W_l = (\rho_l, u_l, p_l)$ and $W_{j+1} = W_r = (\rho_r, u_r, p_r)$, as shown in Fig. 1 . The isentropic EOS for the two fluids are $p = p_l(\rho, s_l)$ and $p = p_r(\rho, s_r)$, where s_l and s_r are the respective constant entropies on the left and right sides of the interface. According to the first assumption, only the two half fluid cells nearest to the interface are involved in the interaction, and the interface position remains changed (see Fig. 1). After the interaction, the interface takes on the interface velocity u_I and pressure p_I. The densities of the two fluids near the interface have also changed to $\rho_{I,l}$ and $\rho_{I,r}$, respectively.

With the method of characteristics, we have the relations

$$u_I = u_l - \int_{p_l}^{p_I} \frac{dp}{\rho_{l,s} c_{l,s}}, \tag{5}$$

$$u_I = u_r + \int_{p_r}^{p_I} \frac{dp}{\rho_{r,s} c_{r,s}}, \tag{6}$$

$$p_I = p_l(\rho_{I,l}, s_l), \tag{7}$$

$$p_I = p_r(\rho_{I,r} s_r), \tag{8}$$

where $\rho_{l,s}$, $c_{l,s}$ and $\rho_{r,s}$, $c_{r,s}$ are the densities and sound speeds determined by the isentropic EOS. The unknown variables u_I, p_I, $\rho_{I,l}$ and $\rho_{I,r}$ can be obtained by solving equations Eq. 5 to Eq. 8. In Appendix A.1, the detailed method for the gas-gas and gas-water interface conditions are described. On the other hand, as the interface velocity has been computed at the interface, the zero level set is then moving at the exact interface velocity. Therefore, we update the zero level set function with solved interface velocity.

3.2 Defining the ghost cells

Suppose the real cell state $W_l = (\rho_l, u_l, p_l)$ in the left cell j interacts with the ghost cell state $W_{gl} = (\rho_{gl}, u_{gl}, p_{gl})$ in the right cell $j + 1$, as shown in Fig. 2. Both the real and ghost cells are treated with the same EOS as for the left medium. The same assumptions are also applicable to the ghost interaction at the cell wall $j + 1/2$ which takes on the functional role as the interface. After the ghost interaction, the interface assumes the velocity u_g and pressure p_g. The densities of the two sides near the cell wall are also changed to $\rho_{g,l}$

and $\rho_{g,gl}$, respectively. We set the interface velocity, pressure and density on the real fluid side to be equal to those after the real interaction, i.e. $u_g = u_I$, $p_g = p_I$, and $\rho_{g,l} = \rho_{I,l}$; this implies that both the ghost and real interaction give the same interface condition for the real fluid. Therefore, the ghost cell states can be obtained by solving

$$u_I = u_{gl} + \int_{p_{gl}}^{p_I} \frac{dp}{\rho_{gl,s} c_{gl,s}}, \tag{9}$$

$$p_{gl} = f_s(\rho_{gl}, s_{gl}), \tag{10}$$

with the given interface condition of u_I and p_I. Here $\rho_{gl,s}$ and $c_{gl,s}$ are the density and sound speed determined by the isentropic EOS on the left medium, and s_{gl} is the ghost cell entropy throughout the interaction. However, one would note that there is no unique solution for the ghost interaction problem. While Eq. 9 and Eq.10 are satisfied, the ghost cell states may be different by choosing various combinations of two variables from density, pressure or velocity. Here, we shall consider two simplest cases:

- *Algorithm A*
  We define the ghost cell pressure as that at the interface after the real interaction, i.e.

  $$p_{gl} = p_I. \tag{11}$$

  Hence the integral in Eq. 9 becomes zero and the ghost cell velocity is

  $$u_{gl} = u_I. \tag{12}$$

  Furthermore, one can find that any ghost cell density can satisfy Eq. 9. We define the ghost cell density by isentropic extrapolating, i.e. $s_{gl} = s_l$. Therefore, the ghost cell density on the right side can be computed directly by $p_{gl} = f_s(\rho_{gl}, s_l)$. See Appendix A.2 for details on gas-gas and gas-water interactions.
- *Algorithm B*
  We define the ghost cell pressure and density by constant extending, i.e.

  $$p_{gl} = p_l, \tag{13}$$

  $$\rho_{gl} = \rho_l. \tag{14}$$

  Hence, from Eq. 5 and Eq. 9, we obtain the ghost cell velocity as

  $$u_{gl} = 2u_I - u_l. \tag{15}$$

As the real and ghost fluids have the same pressure after the ghost interaction (see Fig. 2), via isentropic condition, we have

$$\rho_{I,l} = \rho_{g,gl} \tag{16}$$

for both Algorithm A and B. One can find further that the above two cases are equivalent for the ghost interactions because both the real and ghost fluid give rise to the same interface conditions of velocity, pressure and densities. It may be noted that the ghost cell states in Algorithm B has the same form of the boundary conditions for a moving piston (Hirsch, 1990; Fedkiw et al, 1999a). Therefore, one may interpret that the physical meaning or outcome of the two algorithm as if the interface is treated as a piston and the velocity of the moving piston is determined by the interface interaction. As the method of characteristics is an approximate Riemann solver, the ghost cell states as enunciated by the Algorithm B may face numerical difficulties associated directly with the accuracy of the calculated interface velocity u_I; for example, when there is a strong rarefaction wave giving rise to the so called "1-2-3" problems (Toro, 1997). In our implementation, we only use Algorithm A to determine the ghost cell states as it is, in practice, numerically more stable.

Similarly, for the real cell state $W_r = (\rho_r, u_r, p_r)$ in cell $j + 1$, the ghost cell state $W_{gr} = (\rho_{gr}, u_{gr}, p_{gr})$ in cell j can also be defined by a ghost interaction with the EOS on the right. It is also noted that, to avoid "over heating" errors, an isobaric fix (Fedkiw et al 1999a) can be introduced from $j - 1$ to j and $j + 2$ to $j + 1$ before solving the interface interaction problem. For nodes to the left of j or the right of $j + 1$, the ghost states are simply extended or isentropic extrapolated from W_{gl} and W_{gr}, respectively. Choosing either presents no significant difference for the final results.

In the present method, as the ghost cell density is different from the real density, there is strictly no conservation kept at each time step. However, we expect the conservation error can be reduced or mitigated because the conservation properties is also controlled by a moving piston boundary condition. This will be discussed further in Section 6.4 based on specific numerical examples.

4 Implementation in multidimension

For one dimension, the above interface interaction method is simple and easily implemented. For higher dimensions, as more velocities components are involved, we only need to consider the interface interaction in the normal direction to the interface and hence the normal velocity component is required.

8

In the procedure below, with respect to the direction normal to the interface (or interaction), we shall define the cells with $\phi < 0$ as on the left and the cells with $\phi > 0$ as on the right.

1 Extend p, ρ, u, v along the normal direction to the ghost cells in a narrow band near the interface for the two fluids using Eq. 4.
2 Calculate the normal velocities of the all the cells in the narrow band.
3 Solve the interface conditions for the real interaction along the normal direction via Eq. 5 to Eq. 8.
4 Compute the ghost cell state values by solving the ghost interaction given in Eq. 10 to Eq. 12.
5 Update the ghost cell velocity components by replacing the normal velocity components obtained from the ghost interaction.
6 Update the real cell values of the two fluids separately using the respective one-phase solvers.

5 Modification of re-initialization

In order to minimize or avoid the re-initialization errors as reflected on the interface location, the re-initialization of the level set function is to be modified. As the interface velocity has been computed at the interface, the zero level set is then moving at the exact interface velocity. Therefore, the values of level set near to the interface do not need to be re-initialized. However, as the definition of the narrow band is based on the level set value, the re-initialization is needed for the level set values away from narrow band to maintain as a signed distance to the interface. The re-initialization procedure with the main solver is given as follows:

1 Calculate the interface conditions for all cells in the narrow band and set the calculated interface velocity for level set updating.
2 Set the ghost cell values, and update the whole flow fields.
3 Update the level set via Eq. 2.
4 Re-initialize the level set via Eq. 3 for cells with $\phi > dl$; here $dl = \sqrt{\Delta x^2 + \Delta y^2}$.

The TVD-Runge-Kutta method (Shu and Osher, 1988) may be used for time integration where a full time-step is made up of several sub-time-steps. While the interface condition and the ghost cell values may be computed at every sub-time-step, the the level set updating and re-initialization are computed once in the full time-step.

It is to be noted that Fedkiw et al (1999c) presented a similar method which defines the level set velocity as the velocity of detonation and deflagration waves. However, our treatment here is for a general interface evolution and

the interface velocity extending is also not needed. On the other hand, as the calculated interface velocities in the narrow band are very close, the τ-steps ($\tau = \frac{\Delta x}{2}$) for Eq. 3 can be reduced comparing to that of the GFM (Fedkiw et al, 1999b). Usually, one can only requires about 5 τ-steps to give a good signed distance function.

6   Numerical examples

The following numerical examples are provided to illustrate the ability of the interface interaction method to handle fluids with large difference of states and material properties at the interface. We denote the original ghost fluid method as GFM, the single fluid method as SFM, the modified ghost fluid method as M-GFM and the present interface interaction method as I-GFM. For all the test cases, the one-phase calculations are carried with 5th order WENO-LF(Jiang and Shu, 1996) and 3rd order TVD Runge-Kutta (Shu and Osher, 1988). Before the three sub-time-steps of TVD-Runge-Kutta, the interface condition is solved once. In the one dimensional examples, the number of grid points is 200 and the referenced exact solution is sampled on 200 grid points too.

6.1   Shock tube problems (I)

In this section, we compute for a series of shock tube problems. The first case is one with moderate numerical stiffness. Then the stiffness of the problems are gradually increased by increasing the difference of initial density, pressure or heat ratio at the interface. In all the computations, the initial velocity at the interface is taken as null value.

6.1.1   Case I-A

We consider a air-helium shock tube problem with the following initial data:

$$(\rho, u, p, \gamma) = \begin{cases} (1, 0, 1, 1.4) & \text{if } x < 0.5 \\ (0.125, 0, 0.1, 1.667) & \text{if } x > 0.5 \end{cases}. \tag{17}$$

The typical results at time $t = 0.15$ computed with the I-GFM, GFM, SFM and M-GFM are shown in Fig. 3 , Fig 4 ,Fig. 5 , and Fig. 6 , respectively.

One can observe that the results by I-GFM, GFM and SFM are in good agreement with the exact solution; in particular they have almost identical

and correct shock strength and speed. The interface position is also captured accurately. Both the GFM and I-GFM give a sharp density discontinuity at the interface. However, as the ghost cell density is copied directly from the real fluid, the SFM predicts a perceptibly smeared out density profile while the heat ratio γ discontinuity indicates the interface position.

For the results of M-GFM, one can find the shock front and interface locations are both wrongly predicted and there are large errors pertaining to the rarefaction wave. In the calculation, the interface pressure is chosen from the right and the velocity from the left. If the interface pressure is chosen from the left and the velocity from the right, the results are even worse (not shown here). This example highlights the problems/difficulties faced by M-GFM when the difference in the sound impedance of two fluids is not large as that encounter and originally developed for the gas-water interface by Fedkiw (2002). Further numerical tests also depict large deviations from the exact solution or even unreasonable results obtained by the M-GFM for gas-gas problems (not shown here). For this reason, for the subsequent examples of gas-gas interaction, only the results by I-GFM, GFM and SFM are discussed.

6.1.2 Case I-B

We compute a more stiff shock tube problem where the initial pressure difference is much larger and which is taken from from Abgrall and Karni (2001). The initial data is

$$(\rho, u, p, \gamma) = \begin{cases} (1, 0, 500, 1.4) & \text{if } x < 0.5 \\ (1, 0, 0.2, 1.667) & \text{if } x > 0.5 \end{cases}. \tag{18}$$

The results at time $t = 0.015$ using the I-GFM are shown in Fig. 7 and are in good agreement with the exact solution.

The results obtained with the GFM and SFM are shown in Fig. 8 and Fig. 9 , respectively. For the GFM, even though the general shock strength and speed and the interface position are calculated correctly, there are some discrepancies found near the interface. There is more numerical viscosity produced for the SFM, which leads to greater smearing at the shock front; it requires a much finer distribution of about 800 grid points to ensure sharper shock front comparable to that of the I-GFM or GFM (Abgrall and Karni, 2001).

For both the GFM and SFM, one can also observe the overshoots at the end of the rarefaction waves on the velocity profiles. Abgrall and Karni (2001) suggested that these are due to the difficulties associated with the one-phase solver and not the multifluid modeling. It may be mentioned that, with the I-GFM, the overshoot is replaced by a very mild undershoot even though all

the three methods use the same WENO scheme for the one-phase solver (see the velocity plot in Fig. 7).

6.1.3   Case I-C

For this case, we greatly increase the ratio of initial density by up to an order of magnitude, that is

$$(\rho, u, p, \gamma) = \begin{cases} (1, 0, 500, 1.4) & \text{if } x < 0.8 \\ (10, 0, 0.2, 1.667) & \text{if } x > 0.8 \end{cases}. \tag{19}$$

There is a greater stiffness in the problem due to the larger difference of densities near the interface. We run this case to a final time of 0.025. The results using the I-GFM are shown in Fig 10 . One can find that the results are in reasonably good agreement with the exact solution; the strength and speed of the shock and rarefaction waves and the interface position are calculated accurately.

The results obtained with the GFM are shown in Fig. 11 . Although the calculated interface speed is correct, there are large discrepancies for both the shock and rarefaction waves. Even as the isobaric fix is implemented, a strong "over heat" problem still occurs near the interface. A non-physical wave near the end of rarefaction wave is also produced showing a hump moving from the right to the left. For the SFM, the results shows that both the shock and interface speed are in agreement with the exact solution(see Fig. 12). However, the large numerical viscosity cause much smearing to the shock front. In addition, the discrepancy at the end of the rarefaction wave increases to an almost unacceptable level which produces a large hump in the velocity profile.

6.1.4   Case I-D

In this case, we change the magnitude of density and γ on the right side, such that

$$(\rho, u, p, \gamma) = \begin{cases} (1, 0, 500, 1.4) & \text{if } x < 0.75 \\ (30, 0, 0.2, 2.0) & \text{if } x > 0.75 \end{cases}. \tag{20}$$

As both the initial difference of density and heat ratio at the interface becomes ever larger, this problem is very stiff. Figure 13 shows the typical results by the I-GFM at time $t = 0.02$ depicting still reasonable agreement with the exact solution.

The results obtained with the GFM are shown in Fig. 14 . One can easily observe that the results are almost unreasonable. The speed and strength of the

shock and rarefaction waves as well as the interface position bear much differences from the exact solution. For SFM, the program faces much difficulties and fails to produce meaningful results even at the early stage of computation.

6.2 Shock interface interaction problems (II)

In this section, problems on shock interface interaction are computed. In all the cases considered, a shock wave on the left propagates towards another material medium on the right. As the shock wave makes impact on the interface, the transmitted waves is always a shock wave. For the reflection wave, a shock or rarefaction wave may materialize depending on the shock impedance difference at the interface. Here, the first case gives rise to rarefaction wave at the interface, and the subsequent two cases leads to the formation of reflected shock wave.

6.2.1 Presence of reflected rarefaction wave: Case II-A

We consider a strong shock wave with a pressure ratio of 1000 propagating from a high density gas to a low density gas. The initial data is similar to that from Liu et al (2002) except that the present density ratio is even higher:

$$(\rho, u, p, \gamma) = \begin{cases} (3.984, 27.355, 1000, 1.667) & \text{if } x < 0.5 \\ (0.01, 0, 1, 1.4) & \text{if } x > 0.5 \end{cases}. \tag{21}$$

The exact solution of this problem includes a rarefaction wave reflecting into the high density gas and a shock wave is transmitted into the low density gas. The typical results shown at $t = 0.001$ using I-GFM are plotted in Fig. 15 . The comparison with exact solution shows good agreement.

The results using the GFM and SFM are shown in Fig. 16 and Fig. 17 , respectively. For both method, there is fairly large discrepancy of the calculated interface position and shock wave speed when compared to the exact solution. It is also apparent that the GFM depicts large undershoot or overshoot towards the reflected rarefaction wave end (see the pressure and velocity plots in Fig. 16).

6.2.2 Presence of reflected shock wave: Case II-B

We consider a strong shock wave with a pressure ratio of 100 propagating from a helium-like gas to an air-like gas. The initial conditions are very similar to that taken from Liu et al (2002) except that the density ratio is more severe

with much larger quantity pertaining to the air-like gas. The initial data is

$$(\rho, u, p, \gamma) = \begin{cases} (0.384, 27.077, 100, 1.667) & \text{if } x < 0.6 \\ (10, 0, 1, 1.4) & \text{if } x > 0.6 \end{cases}.$$ (22)

As the shock impedance on the right medium increases with density, it gives rise to a much stronger transmitted and reflected shock waves as the initial shock wave makes impact on the interface. The results obtained at time $t = 0.04$ using the I-GFM are shown in Fig. 18 . The results compare well with the exact solution.

The results computed using GFM and SFM are shown in Fig. 19 and Fig. 20, respectively. The GFM predicts an incorrect transmitted shock speed and interface speed. For the SFM, besides the calculated interface and shock front which exhibiting large degree of smearing, both the computed reflected and transmitted shock waves speed also indicate large discrepancies with the exact solution.

6.2.3 Presence of reflected shock wave: Case II-C

The initial density ratio at the interface is increased by another order of magnitude together with an increase of the heat ratio . The initial condition is given as

$$(\rho, u, p, \gamma) = \begin{cases} (0.384, 27.077, 100, 1.667) & \text{if } x < 0.6 \\ (100, 0, 1, 3.0) & \text{if } x > 0.6 \end{cases}.$$ (23)

In this case, as the right side material is of much higher density and low compressiblity, the impact of shock on the interface produces a transmitted and reflected shock waves which are more intense than the former Case II-B. Figure 21 shows the results using the I-GFM at time $t = 0.04$. The results still compare very well with the exact solution.

On the other hand, the computation via the GFM faces severe difficulties. It overflows after several time steps and no meaningful result is produced. For the SFM, it can compute for this problem but with much smeared interface and transmitted shock wave front (see Fig. 22).

6.3 Shock interaction with water (III)

In this section, two problems of shock interaction with water are computed. In both cases, Tait's EOS is used for the water medium. The state values

are non-dimensionlized with respect to the property of water at 1 atmosphere and length scale $1m$. Since the GFM and SFM face severe difficulties in these problems, only the M-GFM and I-GFM are used to calculate these cases.

6.3.1   Underwater explosion: Case III-A

This problem is taken from Tang and Huang (1996). The initial conditions are given as

$$(\rho, u, p, \gamma) = \begin{cases} (0.01, 0, 1000, 2) & \text{if } x < 0.5 \\ (1, 0, 1, 7.15) & \text{if } x > 0.5 \end{cases}. \tag{24}$$

In an underwater explosion, the high pressure explosive products bubble expands very rapidly in water. It generates a shock wave into the water and a rarefaction wave is reflected back into the explosive bubble.

Figures 23 and 24 show the computed results using I-GFM and M-GFM at time $t = 0.0008$, respectively. One can find that both methods give essentially the correct shock wave strength and speed in water. The I-GFM, however, presents a more accurate solution for the rarefaction wave than that of the M-GFM; the later depicts a smeared out rarefaction wave which can be attributed to the larger numerical viscosity involved.

6.3.2   Underwater explosion: Case III-B

We increase the energy of the explosives such that the initial pressure ratio is increased by at least one order of magnitude. The initial conditions are

$$(\rho, u, p, \gamma) = \begin{cases} (0.5, 100, 20000, 2.5) & \text{if } x < 0.5 \\ (1, 0, 1, 7.15) & \text{if } x > 0.5 \end{cases}. \tag{25}$$

In this case, due to the expansion of the initially very high pressure explosive products, two shock waves are generated; one propagates into the water and the other is reflected back into the explosive products.

The obtained results at time $t = 0.001$ using the I-GFM and M-GFM are shown in Fig. 25 and Fig. 26 , respectively. For the I-GFM, the strength and speed of the two shock waves are correctly predicted. By comparing to the exact solution, one can find while the M-GFM computes a reasonable strength and speed of the transmitted shock wave, this is not so for the reflected shock wave in the explosive products. A non-physical shock wave back is observed in the explosive products (see Fig. 26).

15

6.4 Conservation and convergence test

In this section, we perform the conservation and convergence tests for the I-GFM. Based on the particular Case I-A, we compute and compare the conservation errors incurred by the I-GFM, GFM, SFM and M-GFM. Then the convergence property of the I-GFM on mesh refinement is calculated and discussed for the other typical Case I-A to Case I-D.

For the above-mentioned Case I-A to Case I-D, the relative mass and energy variations for the separated left medium and right medium during the computation can be simply calculated by

$$V = \frac{(\sum_{j=0}^{j=K^n} U_j^n + f^n U_I^n)\Delta x}{(\sum_{j=0}^{j=K^0} U_j^0 + f^o U_I^0)\Delta x}, \tag{26}$$

where U_j is the mass density or energy density on cell j, U_I is the corresponding quantity at the interface, the superscript o and n are for the initial condition and the nth-time-step values, respectively, K is the number of cells fully occupied by the left or right medium and f is its volume fraction at the interface, which is based on the the zero level set position by linear interpolation. In a similar way, the total mass and energy variations are given as

$$V_{total} = \frac{\left[(\sum_{j=0}^{j=K^n} U_j^n + f^n U_I^n)_{left} + (\sum_{j=0}^{j=K^n} U_j^n + f^n U_I^n)_{right}\right]\Delta x}{\left[(\sum_{j=0}^{j=K^o} U_j^o + f^o U_I^o)_{left} + (\sum_{j=0}^{j=K^o} U_j^o + f^o U_I^o)_{right}\right]\Delta x}. \tag{27}$$

Figure 27 presents the relative conservation variation of the left medium mass, the right medium mass, the total mass and the total energy for Case I-A. For the I-GFM, it gives about the smallest errors or deviation form unity and takes the shortest time to obtain a stable value for the two media. For the GFM, it depicts a relatively larger conservation errors than the I-GFM (for all the four quantities considered) and takes a longer time to reach the stable value. For the SFM, which is supposed to possess the conservation property for the total mass, the total mass calculated indicates a value even closer to unity although there are some fluctuations observed. On the other hand, one may note that there are larger errors involved for the individual medium as compared to I-GFM and GFM. This seemingly contradictory situation may indicate that there is considerable mass transport across the interface and the contact discontinuity is also smeared. For the M-GFM, it shows the largest conservation errors. Needless to say, this is also reflected in the solution which deviates most from the exact solutions among all the methods considered (see Fig. 6).

The relative conservation errors of mass (taken w.r.t. to the initial quantity at $t = 0$) as a function of the number grid points for I-GFM are calculated. The results are summarized in Tab. 1 to Tab 4. In all the cases, we can observe that the errors are reasonably small and converge about linearly with $O(\Delta x)$ with mesh refinement. We can further note that the said convergence rate is fairly independent of the problem ranging from the moderately stiff Case I-A to the extremely stiff Case I-D. Comparing to the convergence rate of SFM in Abgrall and Karni (2001), one can deduce that the I-GFM have a much higher rate of convergence.

It is to be noted that Nguyen et al (2002) presented a fully conservation GFM by a redistribution approach, which is simpler than the full space-time differencing method by Glimm et al (2001). While some results are promising, it remains unclear whether the post-processing step to correct for the conservation errors during the GFM procedure is effective when there is already a large conservation error incurred or worse still when the computations break down in the GFM step. For the I-GFM, as it still predicts a reasonably accurate solution with smaller conservation errors, it seems that a similar post-processing procedure can be effectively incorporated and be developed to be a fully conservative I-GFM as well.

6.5 Collapse of 2-D air cavity collapse in water

To demonstrate the implementation of the I-GFM in 2-D and verify the assembled code, we perform a numerical simulation of an experiment carried out previously by Bourne and Field (1992): a 6mm cylinder air cavity in gelatine/water is impacted by a 1.9GPa shock. The experimental results shows that a very high speed jet is formed which then hit the downstream cavity wall. A very high pressure and temperature are also produced at the impact point of the high speed jet. Bourne and Field also observed luminescence in the interaction process. There have been a number of simulations on cylinder cavity collapse under shock (Grove and Menikoff, 1990; Ding and Gracewski, 1995; Ball et al, 2000). According to Bourne and Field's experiments, the schematic of the problem is given in Fig. 28a . All the boundaries are outflow boundaries with zero gradient. The non-dimensionlized (based on the property of water at 1 atmosphere and length scale $1mm$.) initial data is

$$\begin{cases} (\rho = 1, u = 0, v = 0, p = 1, \gamma = 7.15) & \text{pre-shocked water} \\ (\rho = 1.31, u = 67.32, v = 0, p = 19000, \gamma = 7.15) & \text{post-shocked water} \\ (\rho = 1.2, u = 0, v = 0, p = 1, \gamma = 1.4) & \text{air bubble} \\ \phi = -3 + \sqrt{x^2 + y^2} & \text{level set} \end{cases} .(28)$$

17

Here $\phi \leq 0$ represents the air and $\phi > 0$ represents the water. Figure 28a shows a air cavity of radius 3 at (0,0) is to be impacted by a shock wave initiated at $x = 2.4$. A 400x400 nodes grid is uniformly distributed in the respective x and y directions and the same 5th order WENO-LF is also used as the one-phase solver. Figures 28b, 28c and 28d show the typical density contours at $t = 0.02(2.0\mu s)$, $t = 0.031(3.1\mu s)$ and $t = 0.037(3.7\mu s)$ after the shock wave impinges on the air cavity. The results are in good agreement with Bourne and Field's (1992) observation (their Fig. 5). In Fig. 28b, the reflected incident wave shows an anomalous reflection pattern. One can also see such similar features as obtained by Grove and Menikoff (1990) though for different initial condition. As the cavity collapses the high speed jet is also formed. Figure 28c shows the instance just before the jet making impact on the downstream cavity wall. This result is also in reasonable agreement with the calculations of Ball et al (2000) using a completely different numerical scheme called the free Lagrange method. However, the present calculated highest jet velocity just before the impact is about $2800m/s$ which is some $200m/s$ larger than that reported by Ball et al. As the jet impacts on the down stream cavity wall, Ball et al mentioned that a part of the cavity mass is trapped between the jet nose and cavity wall. However, this is not specifically observed or discussed in the experiments and our numerical results indicate likewise. Our results further show that, after the jet impact, while the resultant strong shock wave interacts with the generated lobes, two secondary jets are also produced (see Fig. 28d); the jets subsequently bisect the lobes again to form 4 separated cavities (not shown here). Finally, when these cavities reaches its smallest volume at about time $t = 4.3\mu s$, the calculated temperature in the collapsed cavities is higher than $10000K$ which may be the reason for the presence of luminescence observed in the experiments.

6.6   Air-helium shock interaction

In this 2-D problem, we compute for a Mach 1.22 air shock wave interaction with a cylindrical helium bubble. Hass and Sturtevat's (1987) experimental results showed that, under the air shock pressure, the helium bubble collapses and a jet is produced. Numerical computations for the same problem can be found in Quirk et al (1996), Lian and Xu (1999) and Bagabir and Drikakis (2001). This problem has also been computed by the GFM (Fedkiw et al, 1999b). Figure 29a shows the schematic of the problem, where the upper and the lower boundaries are reflection boundaries of a solid wall. The left and the right boundary condition are outflow boundaries with zero gradient. The nondimensionlzed (based on the property of air at 1 atm and length scale of

$1mm$) initial conditions are

$$
\begin{cases}
(\rho = 1, u = 0, v = 0, p = 1, \gamma = 1.4) & \text{pre-shocked air} \\
(\rho = 1.3764, u = 0.394, v = 0, p = 1.5698, \gamma = 1.4) & \text{post-shocked air} \\
(\rho = 0.138, u = 0, v = 0, p = 1, \gamma = 1.667) & \text{helium bubble} \\
\phi = -25 + \sqrt{(x - 150)^2 + y^2} & \text{level set}
\end{cases}
, (29)
$$

where $\phi \leq 0$ represents the helium and $\phi > 0$ represents the air, depicting a helium bubble of radius 25 at (0,150) which is to be impacted by a shock wave initiated at $x = 100$. The computation has been carried out with four increasing resolutions of $\Delta x = \Delta y = 2, 1, 0.5, 0.25$; this is also to ensure grid invariance as similarly done in Fedikew et al (1999).

Figure 29b shows the density contour corresponding to $t = 1.238(427\mu s)$ after the air shock makes impact on the helium bubble ($\Delta x = \Delta y = 0.25$). The calculated bubble shape and jet shape are in good agreement with Quirk et al's AMR computed results (their Fig. 9h) and Hass and Sturtevat's (1987) experiment (their Fig. 7h). Comparing to the results of the original GFM (Fig. 30 in Fedkiw et al, 1999b), one can deduce that the I-GFM calculates more accurately the interface details including the jet size and the shape of jet head. This is perhaps to be expected since the interface velocity is accurately calculated and is incorporated directly into the level set evolution. Instabilities are also found at the interface, but, just as in the experiments, they are not as strong as the results of Lian and Xu (1999) (their Fig. 4.2) obtained with a front capturing method. Figure 30 gives the several level sets near the interface at the same time as in Fig. 29b . It is found that while the accuracy of the zero level set location is kept, the initial property of signed distance is preserved by the equal spacing of the neighboring level sets. Finally, Fig. 31 shows the relative variation of the total helium mass during the computation for the four different resolutions. On can find that the mass conservation error is very small and manageable. This is especially so for the smallest grid size of 0.25. From Fig. 3 , the calculated time-averaged relative percentage errors in helium mass by (taken w.r.t. the initial quantity at $t = 0$) our I-GFM are significantly lower than that of the GFM; these values are 0.53%, 0.37%, 0.28%, and 0.12% corresponding to the resolutions $\Delta x = \Delta y = 2, 1, 0.5, 0.25$, respectively (which can be compared to 2.5%, 0.78%, 0.42% and 0.43%, respectively, found in Fedkiw et al, 1999b). These results further indicates that the I-GFM has good conservation properties.

19

7   Concluding remarks

In this paper, we developed an interface interaction method based on solving the real and ghost interface interactions. As the method is constructed and modified with respect to the GFM and level set technique, it is simple for implementation and extension to higher dimensions. In the said method, the interface velocity is accurately calculated and the conservation properties are enhanced by the moving piston boundary condition. A number of numerical examples in one dimension are studied with comparisons to exact solution while two dimensional problems are calculated and compared to experiments and previous methods. The results show that the present method can overcomes various difficulties encountered by the original GFM, SFM and the modified GFM. In addition, the interface location is also calculated more accurately by the modification of re-initialization in the level set updating.

The interface interaction method is performed only in a narrow band of the mesh and hence is very efficient. The computational cost is almost like the original GFM in most cases. Finally, as the states for solving the interface conditions can be approximated by high order extrapolation, our method may suggest a way for higher accurate schemes for multifluids flows.

A Interface interaction method for gas-gas and gas-water interaction

A.1 Interface condition

An ideal gas has the EOS of the form

$$p = (\gamma - 1)\rho e, \tag{A.1}$$

where γ is the heat ratio. The Tait's EOS for water is

$$p = B \left(\frac{\rho}{\rho_o} \right)^{\gamma} - B + A, \tag{A.2}$$

where $\gamma = 7.15$, $B = 3.31 \times 10^8 Pa$ and $A = 1 \times 10^5 Pa$. The isentropic form of ideal gas EOS and the water EOS both can also be written as

$$\frac{f(p)}{\rho^{\gamma}} = const, \tag{A.3}$$

where $f(p) = p$ is for an ideal gas and $f(p) = p + B - A$ is for water. And the equivalent form relating the pressure and sound speed c is

$$S = \frac{2}{\gamma - 1} \ln c + \frac{1}{\gamma} \ln f(p). \tag{A.4}$$

Here S is a constant and $c = \sqrt{\gamma f(p)/\rho}$. To solve the interface condition of Eq. 5 to Eq. 8 can be rewritten as

$$u_I = u_l - \frac{2c_l}{\gamma_l - 1} \left[\left(\frac{f(p_I)}{f(p_l)} \right)^{\frac{\gamma_l - 1}{2\gamma_l}} - 1 \right], \tag{A.5}$$

$$u_I = u_r + \frac{2c_r}{\gamma_r - 1} \left[\left(\frac{f(p_I)}{f(p_r)} \right)^{\frac{\gamma_r - 1}{2\gamma_r}} - 1 \right]. \tag{A.6}$$

Equation A.5 and equation A.6 can be solved by Newton's method easily.

For flows with limited change of density and sound speed across the interface, the integrals in Eq. 5 and Eq. 6 can be linearized to

$$u_I = u_l - \frac{p_I - p_l}{\rho_l c_l}, \tag{A.7}$$

$$u_I = u_r + \frac{p_I - p_l}{\rho_r c_r}. \tag{A.8}$$

Then u_I and p_I can be calculated directly as

$$u_I = \frac{\rho_l c_l u_l + \rho_r c_r u_r + p_l - p_r}{\rho_l c_l + \rho_r c_r}. \tag{A.9}$$

$$p_I = \frac{\rho_l c_l p_r + \rho_r c_r p_l + \rho_l c_l \rho_r c_r (u_l - u_r)}{\rho_l c_l + \rho_r c_r}, \tag{A.10}$$

For air-water interaction with limited change of pressure and velocity across the interface, the linearized form Eq. A.9 and Eq. A.10 degenerates to the modified GFM for the relation $\rho_{water} c_{water} \gg \rho_{air} c_{air}$.

A.2   Ghost cell values

The ghost cell pressure and velocity are directly copied from the interface conditions. The ghost density ρ_{gl} is solved by relation Eq. A.3, that is

$$\rho_{gl} = \rho_l \left(\frac{f(p_{gl})}{f(p_l)} \right)^{\frac{1}{\gamma}}. \tag{A.11}$$
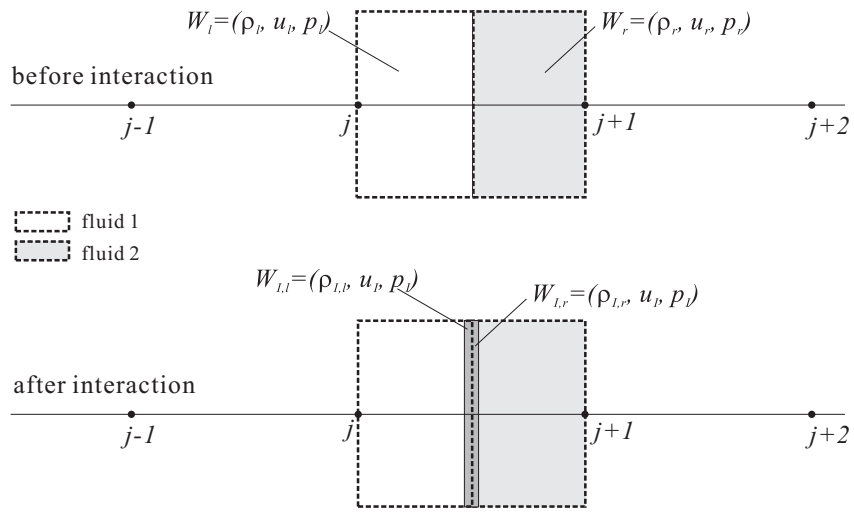
Fig. A.1. Schematic for the interface interaction
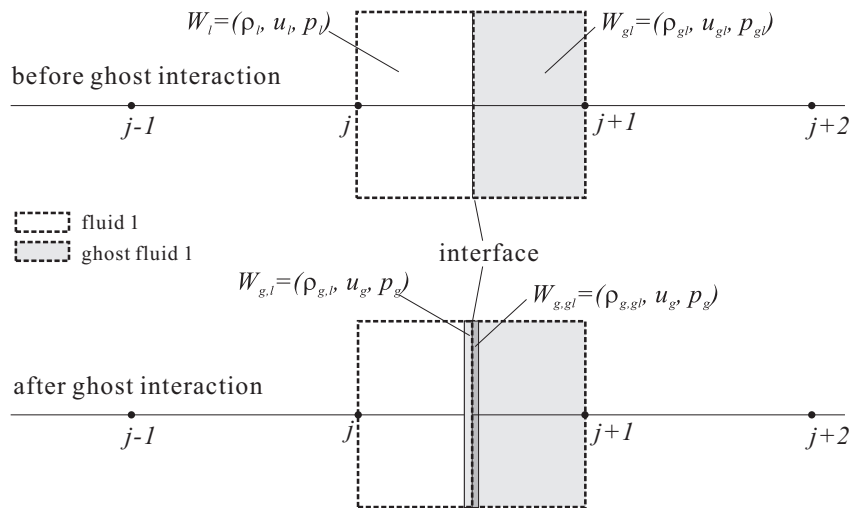
Fig. A.2. Schematic for defining the ghost cells

23
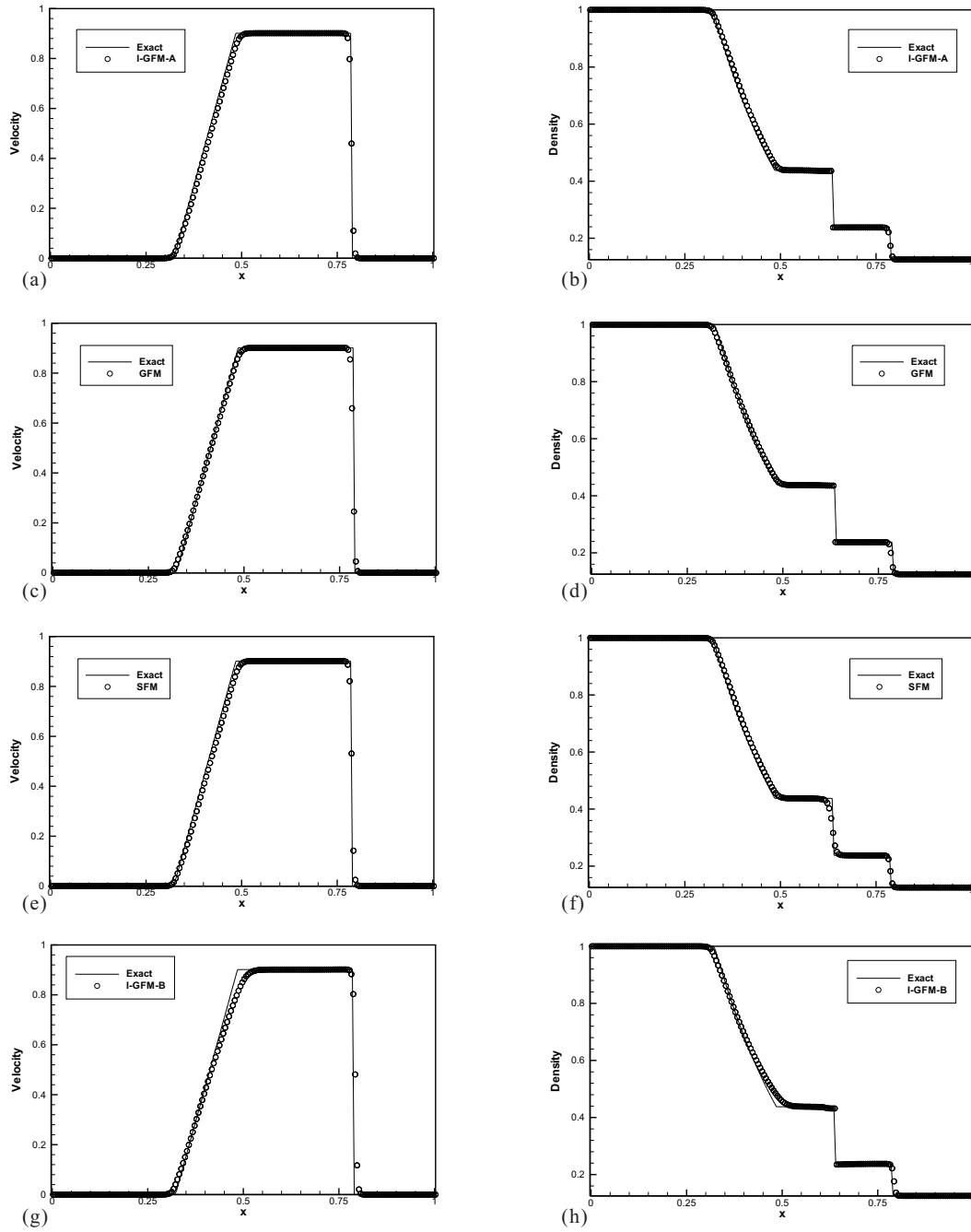
Fig. A.3. Shock tube problem: Case I-A
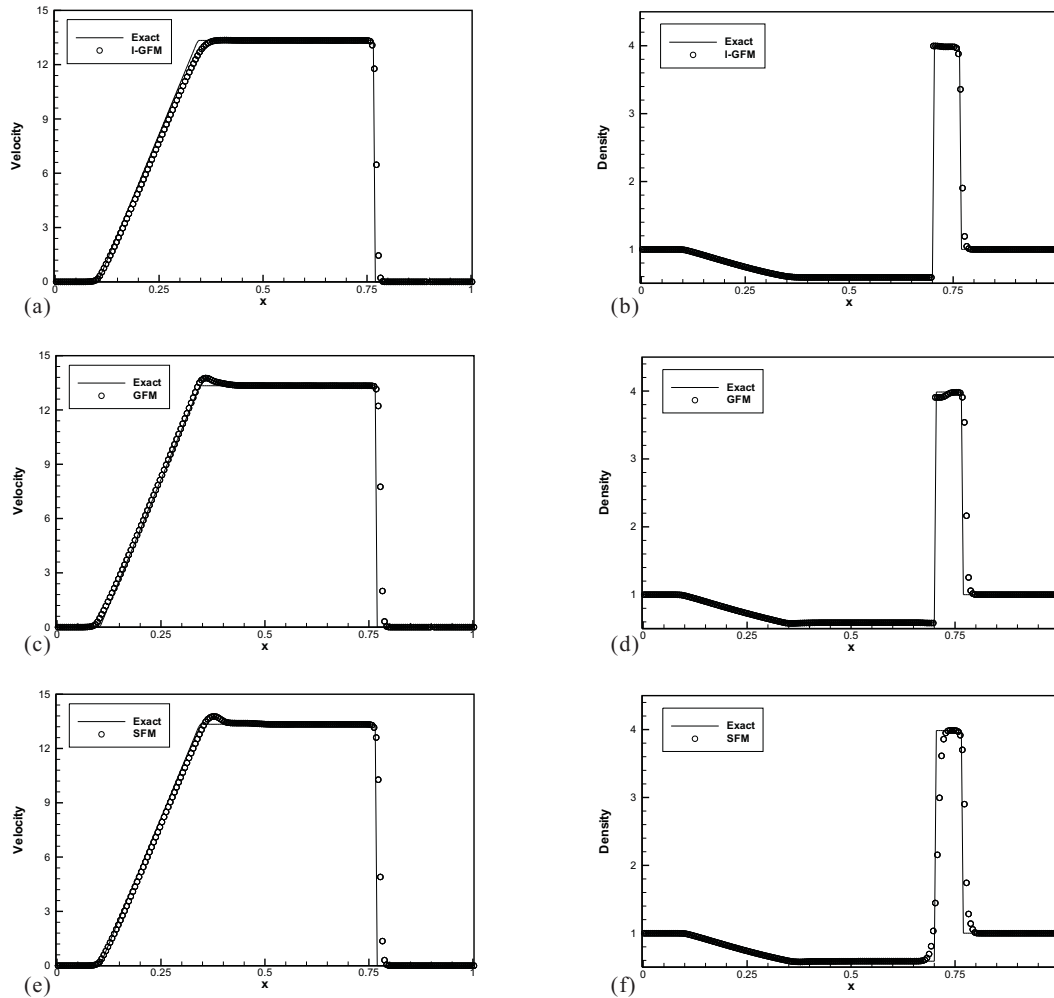
Fig. A.4. Shock tube problem: Case I-B

References

[1] Abgrall R and Karni S (2001) Computations of compressible multifluids. *J. Comput. Phys* **169** 594-623

[2] Bagabir A and Drikakis D (2001) Mach number effects on shock-bubble interaction. *Shock Waves* **11** 209-218

[3] Ball GJ, Howell BP, Leighton TG, Schofield MJ (2000) Shock induced collapse of a cylinder air cavity in water: a free Lagrange simulation. *Shock Waves* **10** 265-276

[4] Bourne NK and Field JE (1992) Shock induced collapse of single cabities in liquids. *J. Fluid. Mech.* **244** 225-240

[5] Cocchi JP and Saurel R (1997) A Riemann problem based method for the resolution of compressible multimaterial flows. *J. Comput. Phys* **137** 265-298
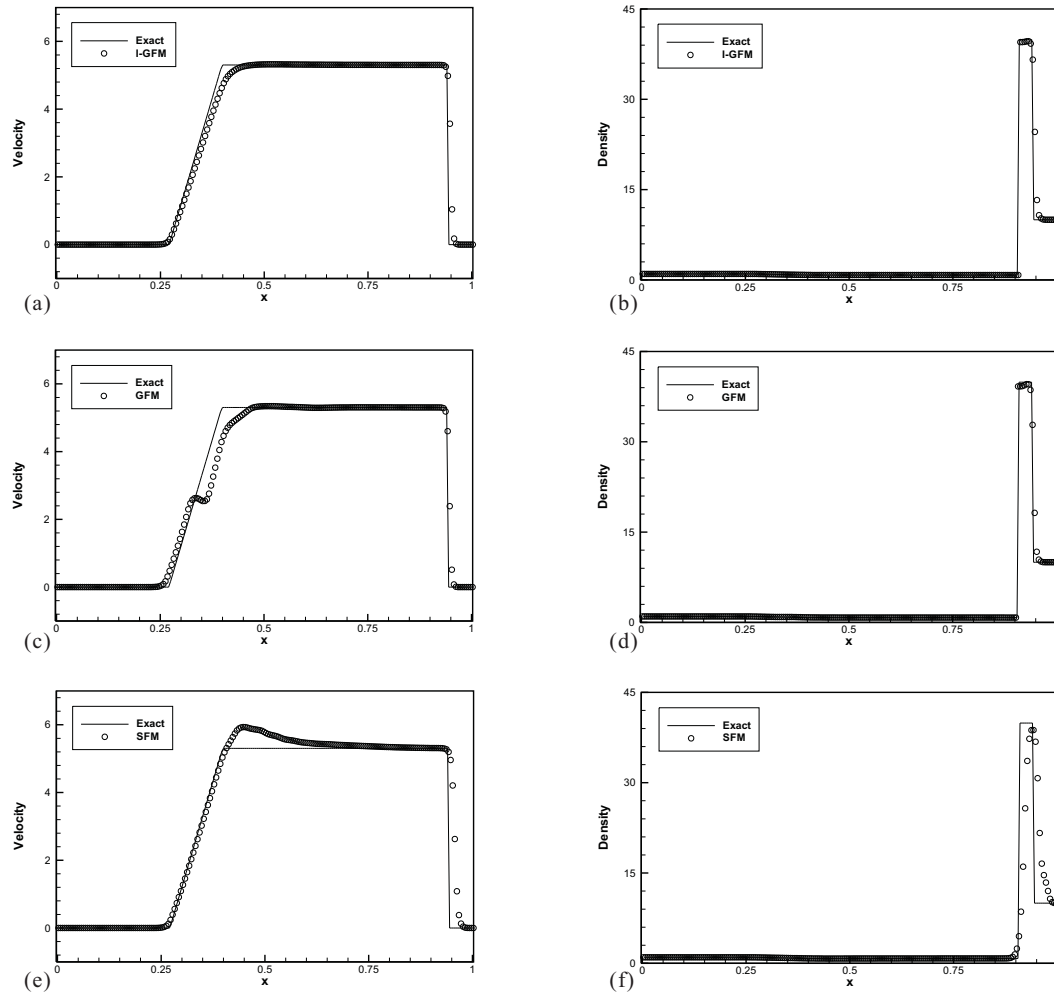
Fig. A.5. Shock tube problem : Case I-C

[6] Davis SF (1992) An interface tracking method for hyperbolic systems of
     conservation laws. *Appl. Numer. Math.* **10** 447-472

[7] Ding Z and Gracewski SM (1995) Behaviour of gas cavity impacted by a weak
     and strong shock waves. *J. Fluid. Mech.* **309** 183-209

[8] Fedkiw R, Marquina A and Merriman B (1999a) An isobaric fix for the
     overheating problem in multimaterial compressible flows. *J. Comput. Phys* **148**
     545-578

[9] Fedkiw R, Aslam T, Merriman B and Osher S (1999b) A non-oscillatory
     Eulerian Approch to interfaces in multimaterial flows (the ghost fluid method).
     J. Comput. Phys **152** 457-492

[10] Fedkiw R, Aslam T, Xu S (1999c) The ghost fluid method for deflagration and
     detonation discontinuities. *J. Comput. Phys* **154** 393-427

[11] Fedkiw R (2002) Coupling an Eulerian fluid calculation to a Lagrangian solid
     calculation with the ghost fluid method. *J. Comput. Phys* **175** 200-224
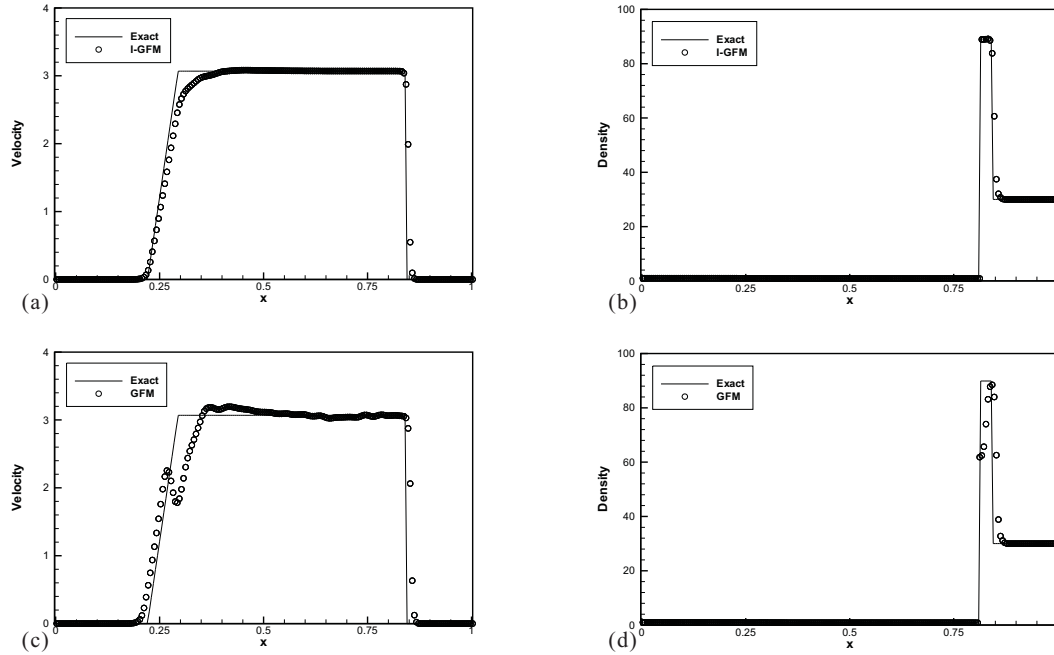
Fig. A.6. Shock tube problem: Case I-D

[12] Glimm J, Marchesin D and McBryan O (1981) A numerical method for two phase flow with an unstable interface. *J. Comput. Phys* **39** 179-200

[13] Glimm J, Grove JW, Li XL and Zhao N (1999) Simple front tracking. In *Contemporary Mathematics, 149. Amer. Math. Soc., Providence, RI* edited by Chen GQ and DiBebedetto E, Volume **238** pages 133-149

[14] Glimm J, Xia L, Liu Y and Zhao N (2001) Conservative front tracking and level set algorithm. *PNAS* **98** 14198-14201

[15] Grove J and Manikoff R (1990) Anomalous reflection of shock wave at a fluid interface. *J. Fluid. Mech.* **219** 313-336

[16] Hass JF and Sturtevant B (1987) Interaction of weak shock waves with cylinderical and spherical gas inhomogeneities. *J. Fluid Mech.* **318** 129-163

[17] Hirsch C (1990) *Numerical Computation of Internal and External Flows,* Vol. 2 (Wiley, New York)

[18] Jiang GS, Shu CW (1996) Efficient Implementation of Weighted ENO Schemes. *J. Comput. Phys* **126** 202-228

[19] Lian Y and Xu K (1999) A gas-kinetic scheme for multimaterial flows and its application in chemical reaction. *NASA/CR 19990-209364*

[20] Liu TG, Khoo BC, Yeo KS (2001a) The simulation of compressible multi-medium flow. Part I: a new methodology with application to 1D gas-gas and gas-water cases. *Comp. & Fluids* **30** 291-314

[21] Liu TG, Khoo BC, Yeo KS (2001b) The simulation of compressible multi-medium flow. Part II: application to 2D underwater shock refraction. *Comp. & Fluids* **30** 315-337
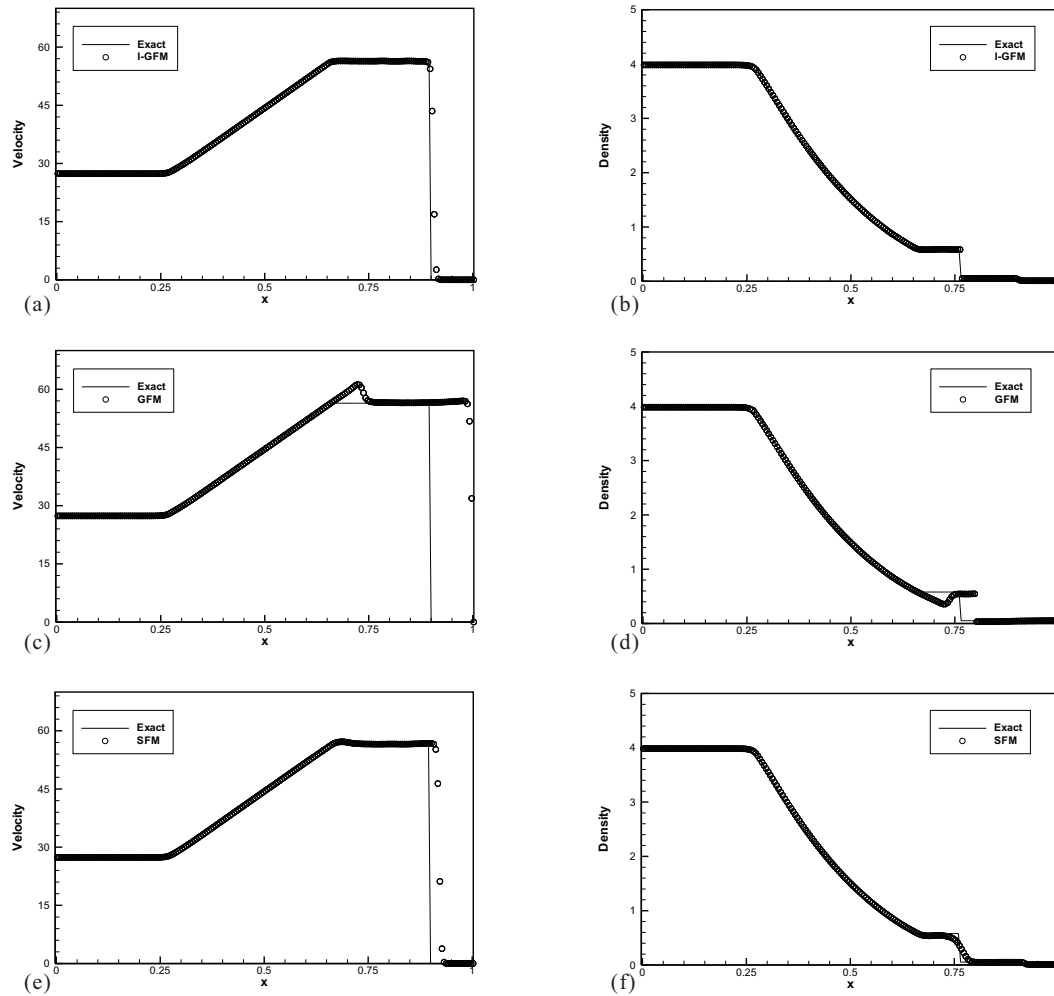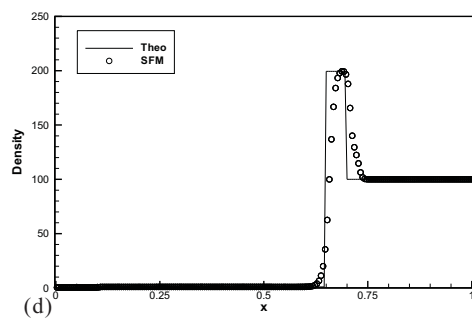
Fig. A.7. Shock interface interaction problem: Case II-A

[22] Liu TG, Khoo BC, Yeo KS (2002) Ghost fluid method for strong shock impacting on material interface. *J. Comput. Phys* submitted for publication

[23] Mudler W, Osher S and Sethian (1992) Computing interface motion in compressible gas dynamics. *J. Comput. Phys* **100** 209-228

[24] Nguyen D Gibou F and Fodfkiw R (2002) A fully conservative ghost fluid method and stiff detonation waves. *12th International Detonation Symposium, San Diego, CA*

[25] Osher S and Sethain JA (1988) Front propagating with curvature dependent speed: algorithm based on Hamilton-Jaccobi formulation. *J. Comput. Phys* **79** 12-49

[26] Peng D, Merriman B, Osher, Zhao H and Kang M (1999) A PDE-based fast local level set method. *J. Comput. Phys* **155** 410-438

[27] Quirk JJ and Karni S (1996) On the dynamics of shock-bubble interaction. *J. Fluid Mech.* **318** 129-163
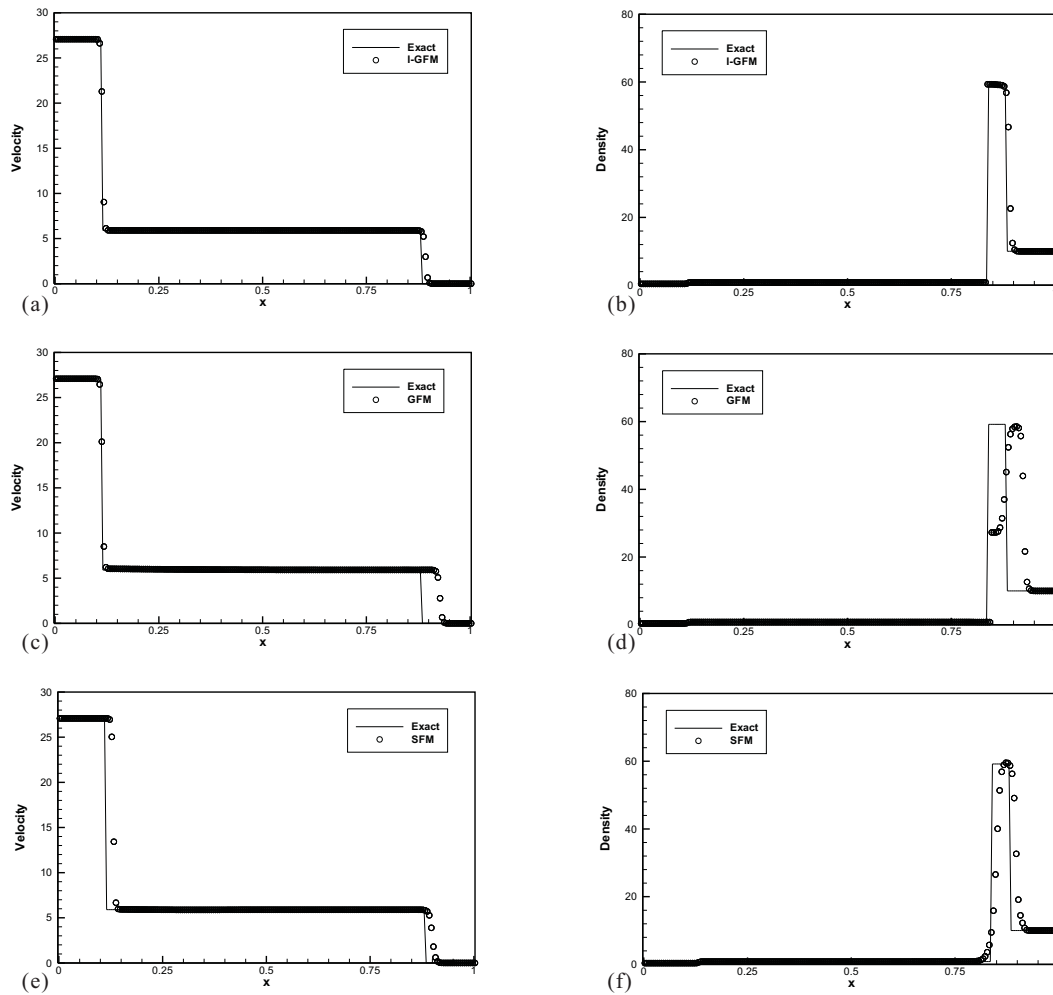
Fig. A.8. Shock interface interaction problem: Case II-B

[28] Rudinger G (1969) *Wave Diagrams for Nonsteady Flow in Ducts* (Dover, New York)

[29] Shu CW, Osher S (1988) Efficient implementation of essentially non-oscillatory shock-capturing schemes. *J. Comput. Phys* **77** 439-471

[30] Sethain JA (1999) Fast Marching Methods. *SIAM Review* **41** 199-235

[31] Tang HS and Huang D (1996) A second-order accurate capturing scheme for 1D inviscid flows of gas and water with vacuum zones. *J. Comput. Phys* **128** 301-318

[32] Toro EF (1997) Riemann solvers and numerical methods for fluid dynamics. Springer Verlag, Berlin
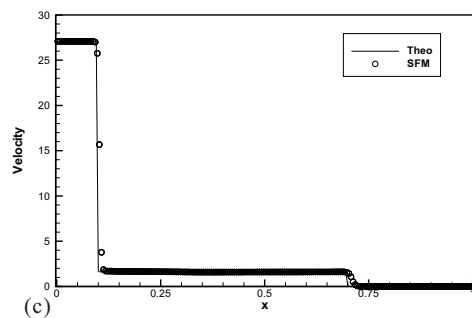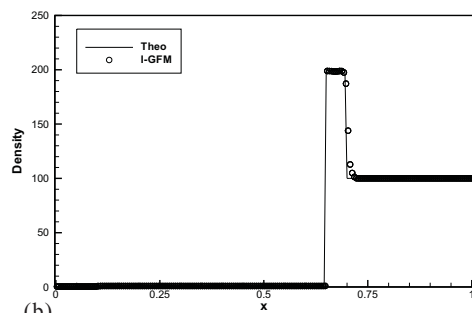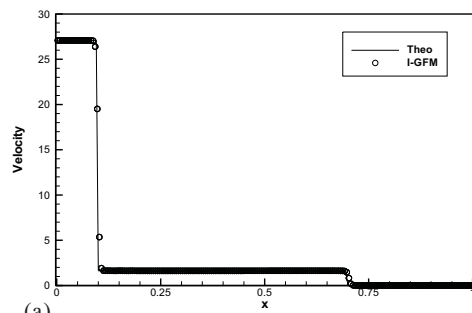
Fig. A.9. Shock interface interaction problem: Case II-C
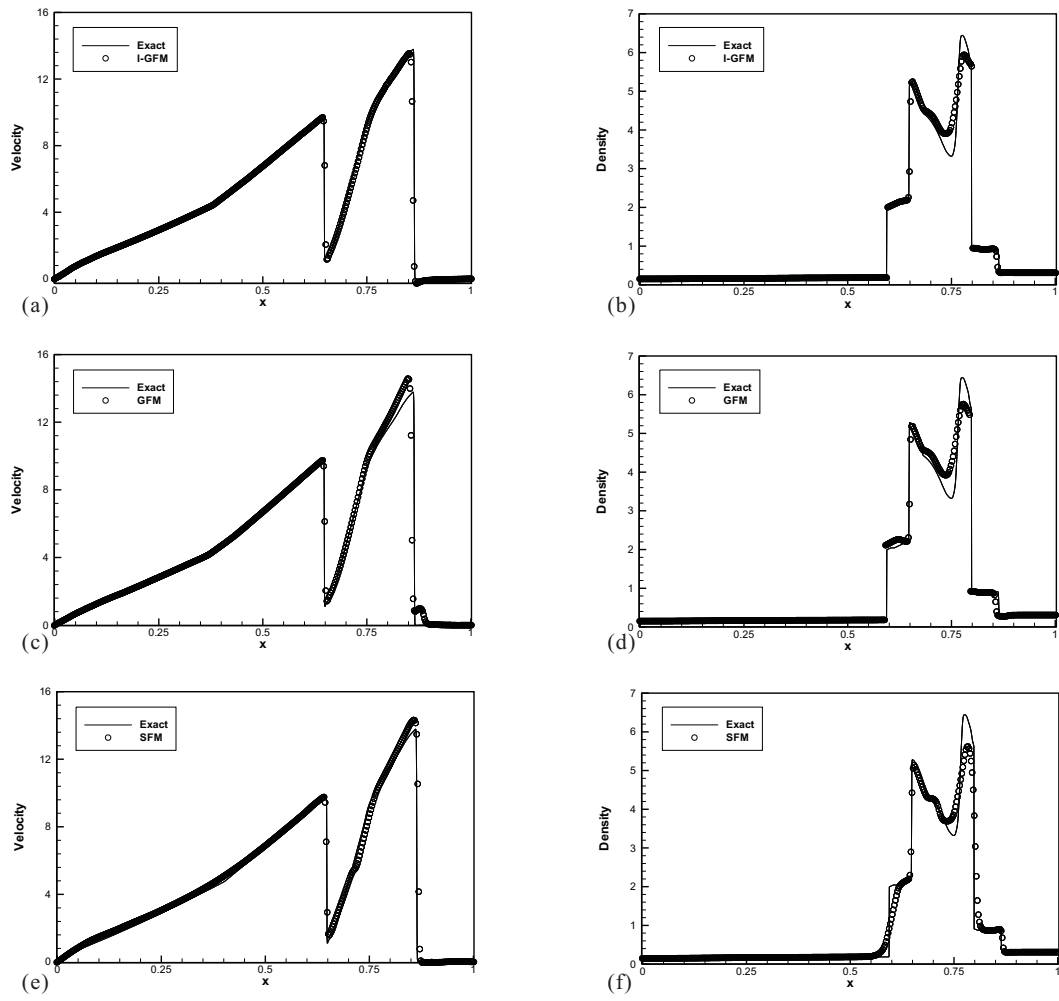
Fig. A.10. Shock interface interaction problem: Case II-D

31
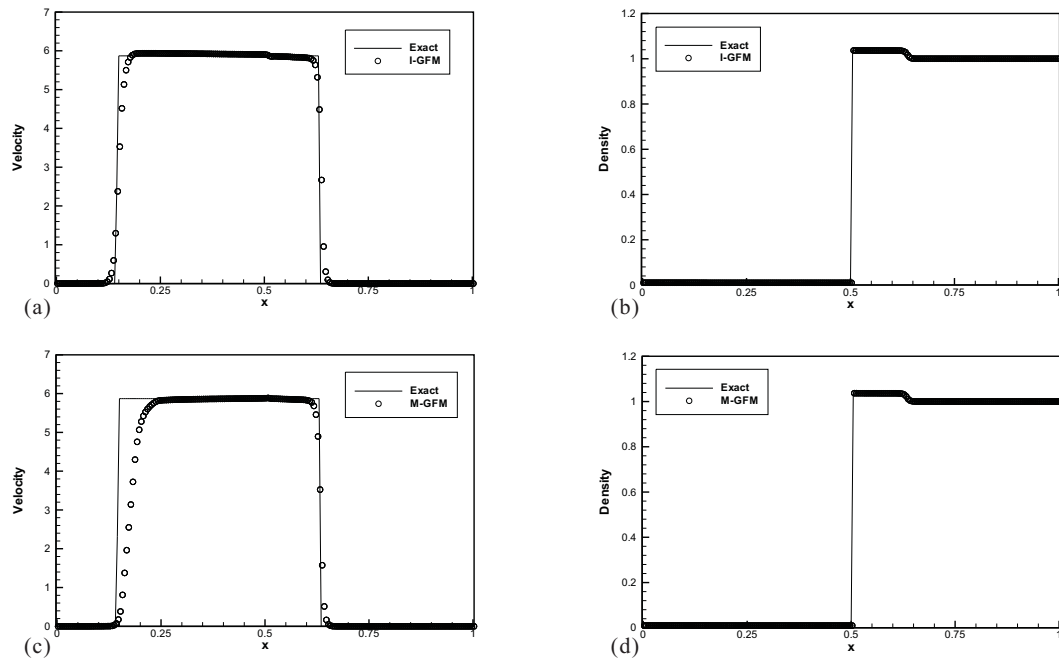
Fig. A.11. Problem on shock interaction with water: Case III-A
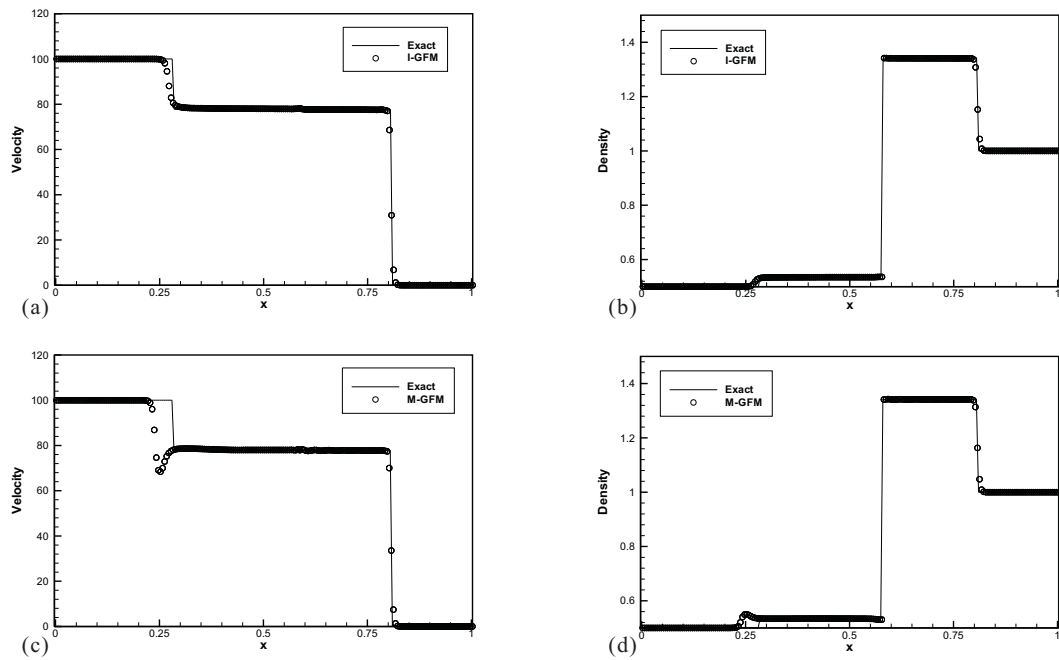
Fig. A.12. Problem on shock interaction with water: Case III-B
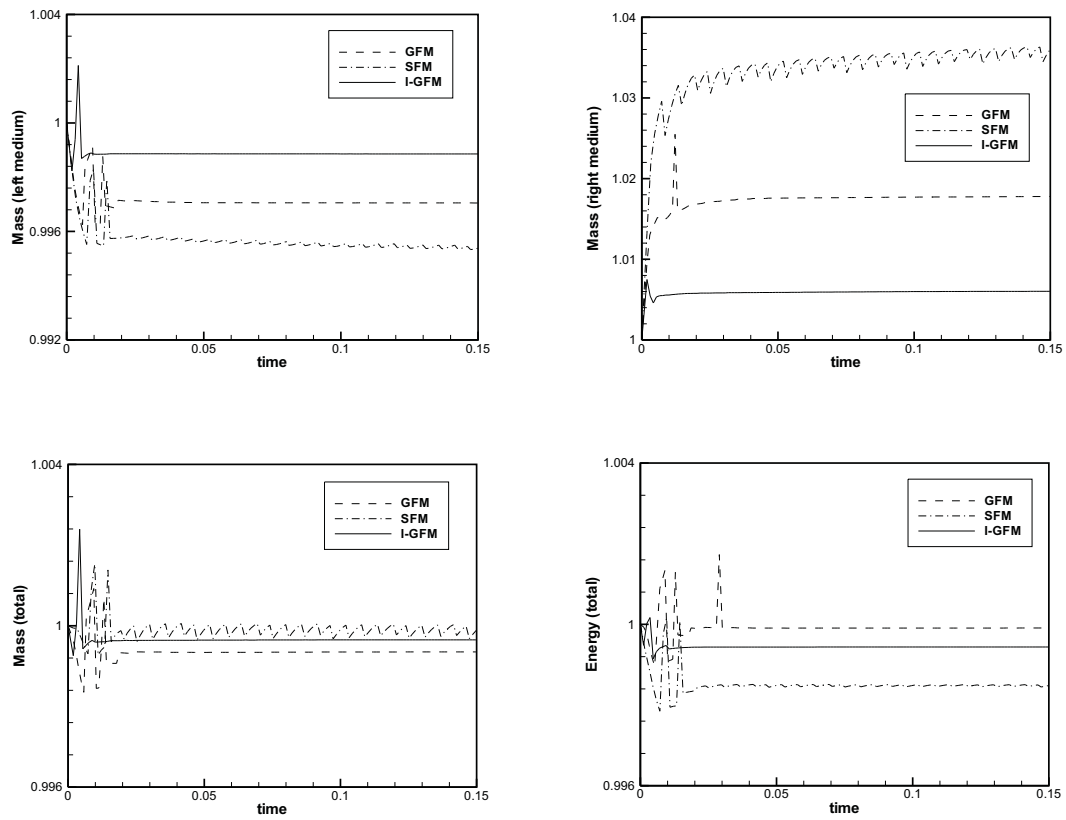
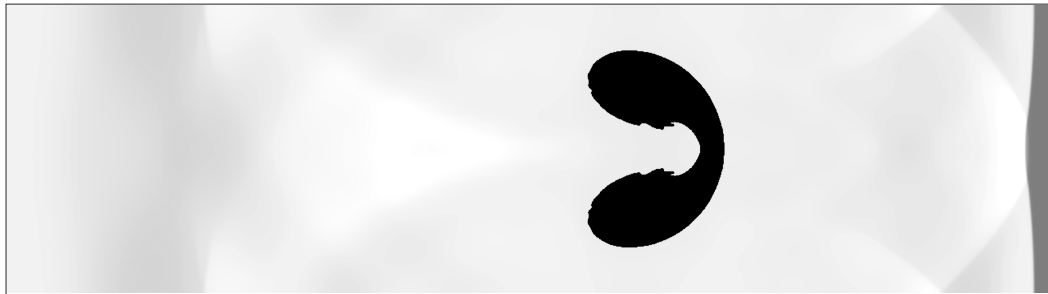Fig. A.13. Relative conservation variation of mass and energy for Case I-A
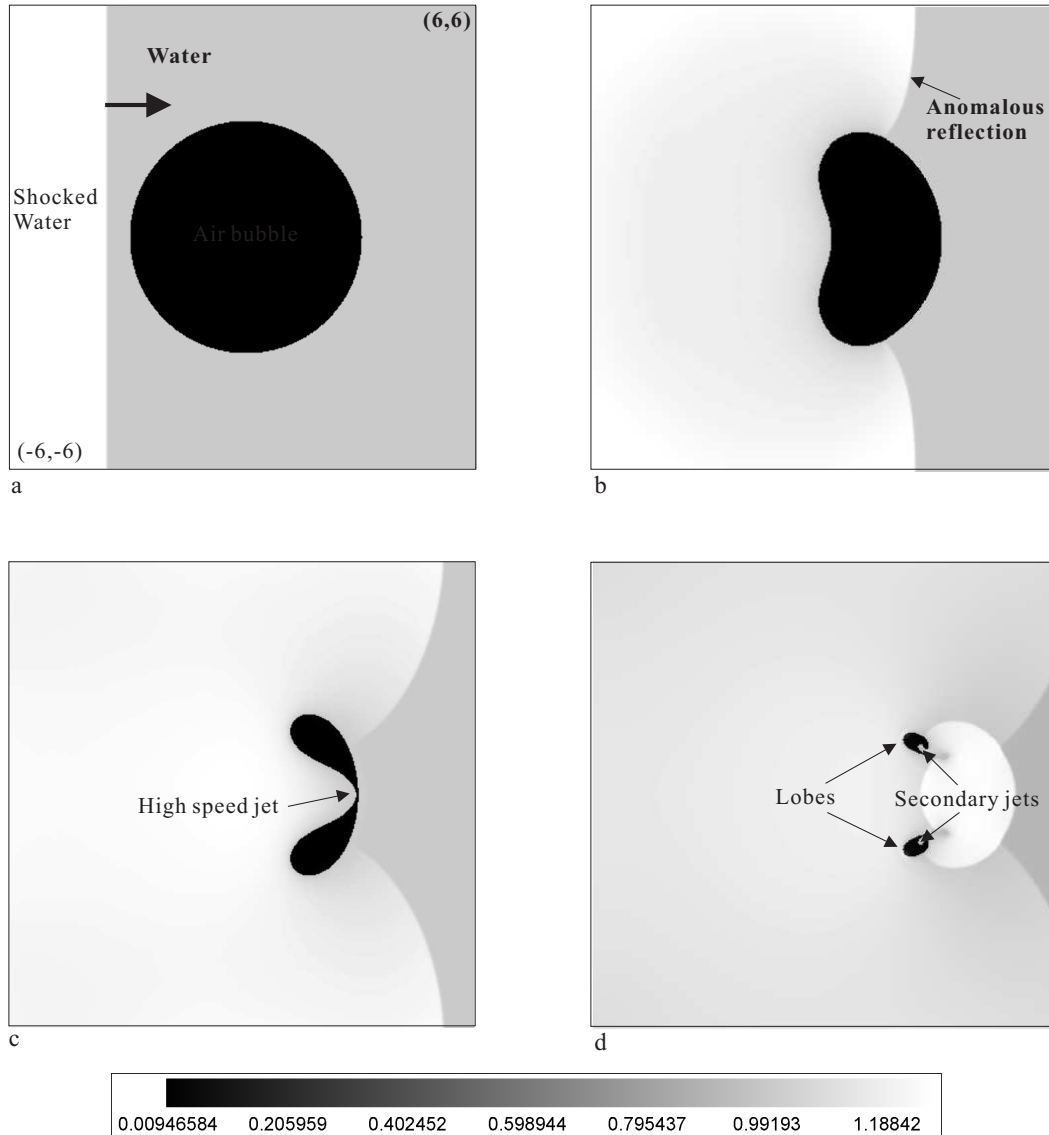
Fig. A.14. Collapse of air cavity in water: a. computational domain and initial conditions, b. density contours at $t = 2.0 \times 10^{-2}(2.0\mu s)$, c. density contours at $t = 3.1 \times 10^{-2}(3.1\mu s)$, d. density contours at $t = 3.7 \times 10^{-2}(3.7\mu s)$
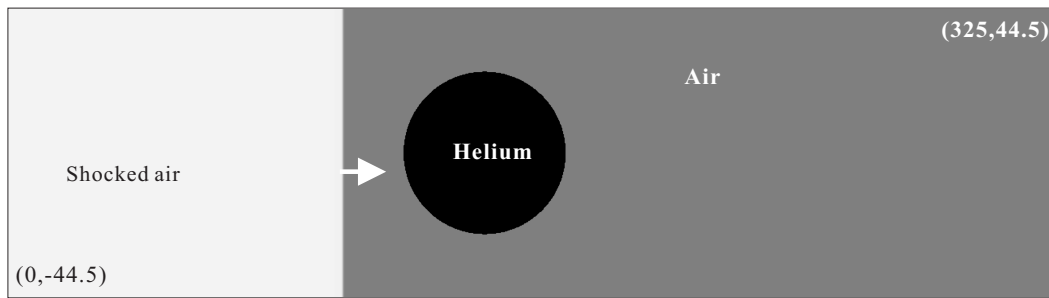
Fig. A.15. Air-helium interaction problem: a. a. computational domain and initial conditions, b. Density contours at $t = 1.238(427\mu s)$
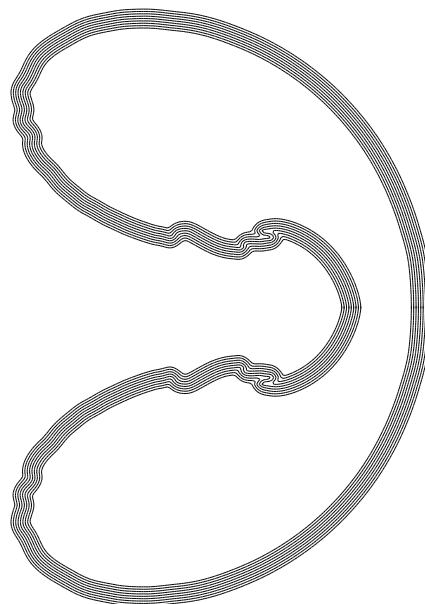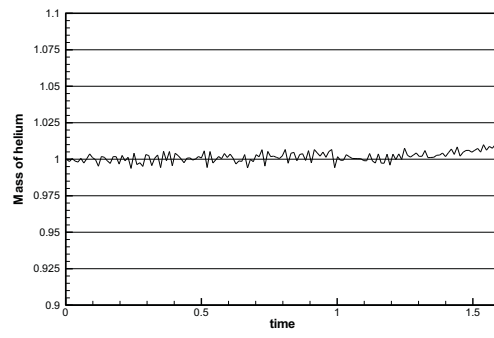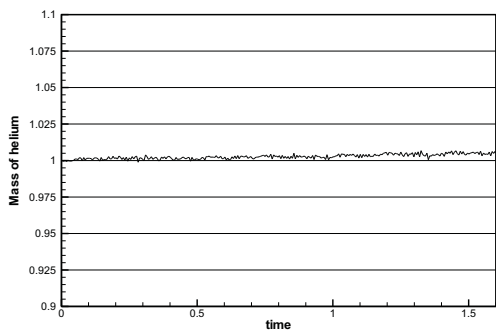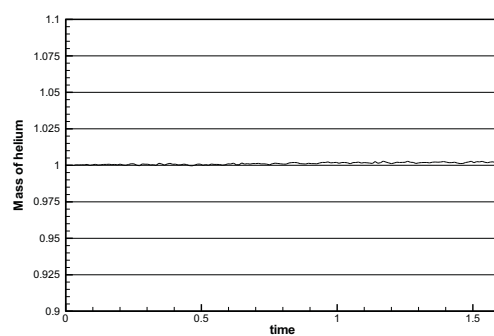

Fig. A.16. Level sets near the interface
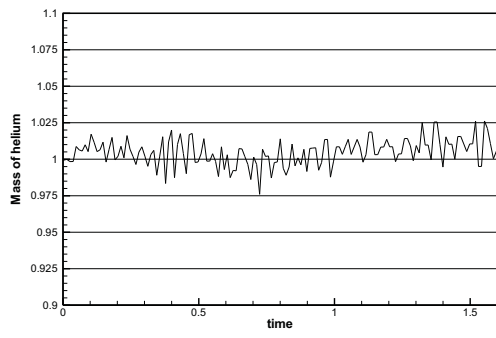
Fig. A.17. Normalized helium mass variation from $t = 0$ to about $t = 1.6(550\mu s)$: a) $\Delta x = \Delta y = 2$, b) $\Delta x = \Delta y = 1$, c) $\Delta x = \Delta y = 0.5$, d) $\Delta x = \Delta y = 0.25$